Five years of Arctic sea ice freeboard measurements from the Ice, Cloud and land Elevation Satellite

Sinead L. Farrell,[1] Seymour W. Laxon,[2] David C. McAdoo,[1] Donghui Yi,[3,4] and H. J. Zwally[4]

Received 7 August 2008; revised 3 February 2009; accepted 18 February 2009; published 23 April 2009.

[1] Using data from the first Earth-orbiting laser altimeter, the Geoscience Laser Altimeter System (GLAS), onboard the Ice, Cloud and land Elevation Satellite (ICESat), we analyze sea ice freeboard in the Arctic Ocean. We describe a new method for sea surface height retrieval, which relies on an algorithm that discriminates laser pulse reflections originating over leads or thin ice. The lead detection algorithm is based on surface reflectivity and analysis of parameters associated with the shape of reflected waveforms. Using knowledge of the local sea surface height and sea ice elevation, we estimate sea ice freeboard and present, for the first time, a time series of Arctic freeboard spanning 5 years between March 2003 and 2008. While the autumn (October–November) and winter (February–March) data illustrate the seasonal and interannual variations in freeboard, following the September 2007 record minimum sea ice extent, the autumn 2007 and winter 2008 spatially averaged freeboards are below the seasonal means at −4.5 cm and −6.8 cm, respectively. Over the observation period, mean freeboard has declined at a rate of ∼−1.8 cm/a during the autumn period and ∼−1.6 cm/a during the winter period, in the region bounded by the northern limit of ICESat coverage at 86°N. Because of the short 5-year observation period, it is unclear whether these results represent a long-term, downward trend in Arctic freeboard or are part of a natural variability. Furthermore, since the variability of snow thickness is included in the ICESat freeboard signal, a decrease in the freeboard cannot wholly be attributed to a decrease in sea ice thickness.

Citation: Farrell, S. L., S. W. Laxon, D. C. McAdoo, D. Yi, and H. J. Zwally (2009), Five years of Arctic sea ice freeboard measurements from the Ice, Cloud and land Elevation Satellite, *J. Geophys. Res.*, *114*, C04008, doi:10.1029/2008JC005074.

1. Introduction

[2] Widespread environmental change within the Arctic climate system has been reported extensively in the recent scientific literature [e.g., *Comiso and Parkinson*, 2004; *Arctic Climate Impact Assessment*, 2005; *Lemke et al.*, 2007]. The Arctic provides an early indicator of global climate change through feedback systems associated with factors such as the high albedo of snow and ice [*Holland and Bitz*, 2003]. Large-scale warming in the Arctic [*Johannessen et al.*, 2004] has resulted in an extension of the length of the summer melt season over sea ice [*Smith*, 1998; *Rigor et al.*, 2000], thawing permafrost [*Osterkamp and Romanovsky*, 1999], and near-coastal thinning and overall shrinkage of the Greenland ice sheet [*Krabill et al.*, 1999; *Lemke et al.*, 2007, and references therein]. Perhaps the most significant change is the diminishing sea ice cover, which is decreasing more rapidly than model predictions [*Stroeve et al.*, 2007]. In September 2007 sea ice extent reached its lowest level since the satellite record began in 1979; the monthly extent, 4.28×10^6 square kilometers, surpassed the previous sea ice minimum record (set in 2005) by 1.28×10^6 square kilometers [*Stroeve et al.*, 2008]. Furthermore, the negative trend in sea ice extent has now shifted from −2.2% per decade for the period 1979–1996, to −10.1% per decade for the period 1996–2007 [*Comiso et al.*, 2008].

[3] Continuous monitoring of sea ice thickness has proved a more difficult task than measuring ice extent; while remote sensing techniques were available since 1979 to routinely map and monitor sea ice extent, the first basin-scale estimates of sea ice thickness using satellite radar altimetry became available just 5 years ago [e.g., *Laxon et al.*, 2003]. There are indications of a reduction in sea ice thickness; submarine-based sonar profiling has revealed that ice thickness in parts of the Arctic has decreased by up to 42% for comparisons of sea ice draft measurements between the period 1956–1978 and the 1990s [*Rothrock et al.*, 1999]. Submarine sonar measurements however are sparse

[1] NOAA Laboratory for Satellite Altimetry, Silver Spring, Maryland, USA.
[2] Centre for Polar Observation and Modelling, University College London, London, UK.
[3] SGT, Inc., Greenbelt, Maryland, USA.
[4] Cryospheric Sciences Branch, Goddard Space Flight Center, Greenbelt, Maryland, USA.

and discontinuous in both space and time, and may not reflect the interannual variability of sea ice thickness and ice advection [*Holloway and Sou*, 2002]. In a recent study *Maslanik et al.* [2007] showed that there has been a significant decline in older sea ice in the Arctic over the last two decades.

[4] Launched in January 2003, the Geoscience Laser Altimeter System (GLAS) on NASA's Ice, Cloud and land Elevation Satellite (ICESat) mission provides high-resolution satellite laser altimetry data (~70 m footprints spaced at 172 m along track) with coverage of the Arctic up to 86°N [*Zwally et al.*, 2002]. Over flat sea ice surfaces the range precision is 2 cm [*Kwok et al.*, 2004; *Zwally et al.*, 2008]. To date, a limitation of the satellite radar altimetry data set is its provision of an only partial sea ice thickness data set for the high Arctic due to nonpolar orbit inclination which limits coverage to 81.5°N. An additional $\sim 2.2 \times 10^6$ km^2 of sea ice is covered by the ICESat orbit configuration, which represents about 15 % of the total ice extent during the winter maximum. Furthermore the GLAS footprint is an order of magnitude smaller than a typical radar footprint (~70 m compared to several kilometers for a radar altimeter) and provides improved spatial sampling of the ice surface.

[5] We use ICESat satellite laser altimeter data to estimate Arctic sea ice freeboard, spanning a 5-year period from March 2003 to 2008, by comparing elevations of open water, or newly refrozen leads, with those of nearby ice floes. ICESat freeboard differs from the radar altimetric measurement of ice freeboard in that it is a measure of both the sea ice freeboard and snow accumulation. This quantity is hereinafter referred to simply as freeboard.

[6] A number of methods to derive freeboard from ICESat data have been presented in the literature. Initial attempts to estimate freeboard, and derive sea ice thickness, were described by *Kwok et al.* [2004], and relied on analysis of ICESat elevation profiles in combination with near-coincident RADARSAT imagery. Techniques to derive freeboard on the basis of the removal of a model of the marine geoid yielded freeboards that were contaminated by remaining errors in the geoid [e.g., *Forsberg and Skourup*, 2005; *Kwok et al.*, 2006]. More recently *Kwok et al.* [2007] and *Zwally et al.* [2008] have described more detailed algorithms for estimation of freeboard over basin scales in the Arctic and the Antarctic, respectively.

[7] Previous studies have shown maps of Arctic sea ice freeboard for select ICESat campaign periods [e.g., *Kwok et al.*, 2007; *Kwok and Cunningham*, 2008]. Here, for the first time, we show Arctic freeboard estimates, spanning the 5 years of operation of the ICESat mission, and we assess the interannual changes in the freeboard distribution. We present a new method for sea surface height retrieval, which relies on an algorithm that discriminates ICESat waveforms originating over leads or thin ice. This lead detection algorithm is distinct from those described by *Kwok et al.* [2007] and *Zwally et al.* [2008], in that it is based on surface reflectivity and analysis of parameters associated with the shape of the reflected waveform. Classification of laser reflections from lead surfaces enables the generation of a reference profile of sea surface height, which when subtracted from the elevations of nearby ice floes yields estimates of freeboard. In addition to cryospheric applications, sea surface height measurements derived using the technique we describe here have a number of geodetic applications, and have been used to map marine gravity anomalies in the Arctic up to 86°N [*McAdoo et al.*, 2008].

[8] In section 2 we describe both the ICESat data products and the additional data sets utilized in our analysis. We discuss the filtering scheme that has been applied to the ICESat data in section 3. In section 4 we introduce a new lead detection algorithm for the retrieval of altimetric sea surface height in the Arctic Ocean, and we outline the procedure to calculate sea ice freeboard. Analysis of Arctic freeboard gathered during 11 boreal autumn and winter ICESat campaigns between March 2003 and 2008 is presented in section 5.

2. Data Description

2.1. ICESat Data

[9] Following the initial calibration and validation (cal/val) phase of the ICESat mission in March 2003 (when the satellite was in an 8-day repeat orbit), ICESat now operates in a 91-day exact repeat orbit with a 33-day subcycle. Laser operation periods last approximately one 33-day subcycle. Between 2003 and 2006, laser operation periods occurred every ~3 months, but since 2007 operation periods occur twice a year so as to extend the life of the laser. These typically span a subcycle between February/March and another between October/November [*Schutz et al.*, 2005]. We present results from 11 ICESat campaigns that take place in the autumn (October–November) and winter (February–March) seasons (Table 1) allowing for analysis of the ice pack (1) just after sea ice minimum which occurs in mid-September and (2) at sea ice maximum in March. We do not include an analysis of the spring campaigns (May/June data) since this is the start of the melt season in the Arctic and data is typically more sparse [*Kwok et al.*, 2006] mainly due to cloud cover. Furthermore difficulty in distinguishing laser pulses reflected by melt ponds from those reflected by leads could pose a problem for the lead-detection algorithm. Throughout we will refer to ICESat campaigns by their campaign name, e.g., ON05 (see Table 1).

[10] ICESat data comprises fifteen separate data products labeled GLAxy, where xy denotes a two-digit number. Parameters relevant to our sea ice analysis include the geolocated footprint location (i_lat, i_lon), elevation (i_elev), reflectivity (i_reflctUncorr), and saturation range correction (i_satRngCorr) from the GLA06 Global Elevation Data Product. For each laser pulse we obtain a record of the transmitted (i_tx_wf) and received (i_rng_wf) waveforms from the GLA01 Global Altimetry Data Product. In addition, we use the detector gain (i_gainSet1064) and received pulse energy (i_RecNrgLast_EU) reported in the GLA01 product. Further descriptions of these parameters are given by *Brenner et al.* [2003].

[11] Standard corrections for tides, and atmospheric delay are applied to the laser data [*Brenner et al.*, 2003]. The mission pointing knowledge requirement of 1.5 arc sec corresponds to 4.5 m horizontal and 2 cm vertical range precision [*Zwally et al.*, 2002], and the accuracy of ICESat elevation measurements may therefore be compromised by inadequate knowledge of beam pointing. Furthermore the lack of a range correction for forward scattering of the laser

Table 1. Summary of Laser Operation Periods and ICESat Data Used in This Assessment[a]

Operation Period	Campaign Name	Start Date	End Date	Days in Operation	Orbit Repeat/Subcycle (days)
L1a	FM03	20 Feb. 2003	21 Mar. 2003	30	8
L2a	ON03	4 Oct. 2003	19 Nov. 2003	47	91/33
L2b	FM04	17 Feb. 2004	21 Mar. 2004	34	91/33
L3a	ON04	3 Oct. 2004	8 Nov. 2004	37	91/33
L3b	FM05	17 Feb. 2005	24 Mar. 2005	36	91/33
L3d	ON05	21 Oct. 2005	24 Nov. 2005	35	91/33
L3e	FM06	22 Feb. 2006	28 Mar. 2006	35	91/33
L3g	ON06	25 Oct. 2006	27 Nov. 2006	34	91/33
L3h	MA07	12 Mar. 2007	14 Apr. 2007	34	91/33
L3i	ON07	2 Oct. 2007	5 Nov. 2007	35	91/33
L3j	FM08	17 Feb. 2008	21 Mar. 2008	34	91/33

[a]The science phase of the mission operates in a 91-day repeat orbit, with a 33-day subcycle. The campaign name is used throughout to identify a particular operation period.

pulse in the presence of cloud cover could result in range errors of 10–20 cm or more, depending on cloud type. Here we use Release 428 data which includes the latest precision orbit determination (POD) and precision attitude determination (PAD) as well as scan maneuver calibrations applied to correct for systematic pointing errors [*Luthcke et al.*, 2005]. A filtering technique (outlined in section 3) is used to discard data that has potentially been affected by forward scattering due to clouds.

[12] Saturated received pulse waveforms, which have clipped peak amplitudes and are artificially wide, have been observed over flat surfaces including ice and standing water [*Fricker et al.*, 2005]. The automatic gain control loop responds too slowly to high received pulse energy, which causes the detector to saturate and distorts the waveform [*Zwally et al.*, 2008]. Saturated waveforms manifest themselves as an increase in the range delay and therefore result in anomalously low-elevation measurements [*Fricker et al.*, 2005]. Following *Kwok et al.* [2007] and *Zwally et al.* [2008], we apply the latest version of a correction for saturation (i_satRngCorr), provided in the Release 428 data products, to those elevation estimates derived from waveforms which were flagged as being moderately saturated. The presence of heavily saturated waveforms within the ice pack could indicate specular reflections from leads with very calm, mirror-like surfaces. However, the R428 saturation correction is not applicable for heavily saturated waveforms and we therefore discard these data from our analysis using the filtering scheme described in section 3.

[13] Since the ocean responds to changes in the atmospheric pressure distribution across its surface through a process known as the inverse barometer effect, we must make a correction to the surface elevation measurements to account for this effect. *Kwok et al.* [2006] found pressure variations of up to 70 mb during a 16-day period across the Arctic Ocean, equivalent to a ~70 cm variation in sea surface elevation. Including an inverse barometer correction significantly reduces the variance of the sea surface measurements [*Kwok et al.*, 2006]. Here we have applied the classic isostatic inverse barometer correction to the ICESat elevations using the surface pressure (i_Surface_pres) provided in the GLA06 product. Following *Gill* [1982], the isostatic inverse barometer correction may be calculated as follows:

$$\Delta h_{\mathrm{IBC}} = 0.009948(P - P_0), \tag{1}$$

where, Δh_{IBC} is the inverse barometer correction in meters, P is local sea level pressure (i_Surface_pres) in millibars, and P_0 is the reference sea level pressure (1013.3 mb).

2.2. Additional Data Sets

[14] The Moderate Resolution Imaging Spectroradiometer (MODIS) imagery used in our analysis was acquired from the L1 and Atmospheres Archive and distribution system (LAADS), which can be found at http://ladsweb.nascom.nasa.gov. MODIS, one of the instruments carried on board the NASA satellites Aqua and Terra, acquires images of the Earth's surface in 36 spectral bands and covers the entire globe every 1 to 2 days. Here we use the MODIS Level 1B Calibrated Geolocated Radiances product, which provides visible imagery with a resolution of 250 m.

[15] As part of our analysis we require a sea ice mask to enable selection of ICESat altimetry data over the sea-ice covered regions of the Arctic Ocean. For this purpose we use Special Sensor Microwave/Imager (SSM/I) sea ice concentrations which are computed from the Defense Meteorological Satellite Program (DMSP) F-13 SSM/I Daily Polar Gridded Brightness Temperatures [*Maslanik and Stroeve*, 2007]. These data are available at the NSIDC website at http://nsidc.org/data/nsidc-0001.html.

3. Data Filtering

[16] Before we begin the task of estimating sea surface heights and calculating sea ice freeboard we remove data that have been affected by severe pulse saturation, forward scattering due to clouds, and other invalid elevations. Our filtering scheme is similar to those described by *Zwally et al.* [2008] and *Kwok et al.* [2007].

[17] First, in order to exclude from our analysis regions of open ocean near the sea ice edge, we only consider areas of the ice pack were the SSM/I sea ice concentration is $\geq$35%. This removes data in the marginal ice zone and accounts for less than 5% of the total data, thus having little impact on our results. In addition, we perform coarse editing of the data set to remove any elevation outliers from our analysis, including contamination by land, ice shelves and ice bergs; this is achieved by excluding elevations that deviate by more than 5 m from the Arctic Gravity Project (ArcGP) geoid [*Kenyon and Forsberg*, 2001; http://earth-info.nga.mil/GandG/wgs84/agp/readme_new.html]. We remove any waveforms where the surface reflection was partially or completely lost from the range window (i.e., the maximum

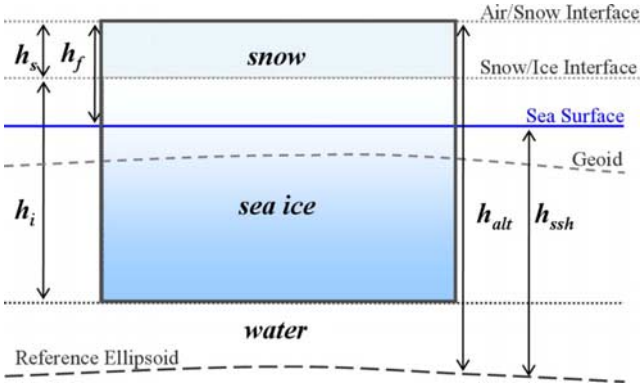

Figure 1. Idealized schematic illustrating a snow covered sea ice flow in hydrostatic equilibrium. Sea ice thickness (h_i), snow thickness (h_s), freeboard (h_f), surface elevation above the reference ellipsoid (h_{alt}), and sea surface height (h_{ssh}) are shown.

amplitude of the waveform was recorded at the very start or end of the range window), as well as waveforms with no discernible signal above the background noise level. Transmission of the laser pulse through thick polar clouds could give rise to waveforms with these characteristics. We discard returns with an unphysical reflectivity >1, since these are likely to be associated with distorted (clipped) waveforms that are the result of detector saturation [*Kwok et al.*, 2006]. Finally we eliminate waveforms which have high gain values. In analysis over Antarctic sea ice, *Zwally et al.* [2008] applied a limit of 80 counts to the detector gain. Following *Kwok et al.* [2007] and *Yi et al.* [2005], we employ a more conservative limit by discarding any waveforms where the detector gain is >30 counts. The detector gain setting is time varying and adjusts depending on the maximum amplitude of the received pulse [*Brenner et al.*, 2003]. High gain values indicate a low signal-to-noise ratio as a result of atmospheric scattering due to clouds, water vapor, etc. [*Kwok et al.*, 2006]. Under the filtering scheme described here, for example, 18% of the FM05 data and 37% of the ON05 data were discarded. The high-gain filter accounts for most of the discarded data and therefore more data is rejected from the autumn campaigns than the winter campaigns because of a higher percentage cloud cover.

4. Detecting Sea Surface Elevations and Measuring Freeboard

[18] The calculation of sea ice freeboard relies upon determining the elevation of sea ice above the water surface. Lead detection is therefore critical since this enables the generation of a reference profile of sea surface height, which when subtracted from the surface elevation of nearby ice floes yields estimates of freeboard. Narrow leads, tens to hundreds of meters wide, and often hundreds of kilometers long, are the predominant site of open water and young ice within the winter Arctic ice pack. Rapid thermodynamic growth of thinner ice maintains a low fraction of open water cover throughout the winter [*Wadhams and Horne*, 1980]. *Maykut* [1978] states that leads represent about 1% of the sea ice pack. RADARSAT Geophysical Processor System (RGPS) measurements of the winter ice pack in the western Arctic during the late 1990s suggest that the coverage of open water and thin ice (<20 cm thick) is less than 2% [*Kwok and Cunningham*, 2002]. Analysis of satellite imagery suggests that the percentage cover of leads and open water within the ice pack varies regionally (sea ice edge compared to multiyear ice pack); *Lindsay and Rothrock* [1995] found that while the lead fraction was 2–3% in the central Arctic during the winter, it was 6–9% in the peripheral seas. Using Upward Looking Sonar (ULS) submarine data, *Laxon et al.* [2003] calculate that the percentage of leads and thin ice also varies seasonally with lead fraction around 10% in October and around 3% in March–April.

[19] Over sea ice, the received laser pulse is treated as a reflection from the air/snow interface [*Giles et al.*, 2007; *Leuschen et al.*, 2008], and provides a measure of the elevation of the top of a sea ice floe with respect to the reference ellipsoid. All ICESat elevations (i_elev) are reported with respect to the TOPEX/Poseidon ellipsoid. Figure 1 illustrates a sea ice floe in hydrostatic equilibrium; sea ice thickness (h_i), snow thickness (h_s), the altimetric surface elevation measurement with respect to the reference ellipsoid (h_{alt}), and sea surface height (h_{ssh}) are shown. We refer to the distance between the surface elevation and the sea surface as the freeboard (h_f), which we define here as the elevation of sea ice, plus accumulated snow, above the sea surface.

[20] The geoid, an equipotential surface which represents the theoretical shape of the ocean surface at rest were there no oceanic or atmospheric circulation, is the main component of the surface elevation measurement (h_{alt}) over the oceans (Figure 1). It can deviate by approximately ±100 m from the reference ellipsoid [*Chelton et al.*, 2001]. In the following analysis we apply the inverse barometer and saturation corrections and subtract a geoid model to obtain surface elevation anomalies (h_a) which have the large amplitude geoid component removed:

$$h_a = h_{\mathrm{alt}} + \Delta h_{\mathrm{IBC}} + \Delta h_{\mathrm{sat}} - h_g, \tag{2}$$

where h_{alt} is the altimetric elevation measurement (i_elev), Δh_{IBC} is the inverse barometer correction (equation (1)), Δh_{sat} is the saturation range correction (i_satRngCorr), and h_g is the ArcGP geoid model. We then operate using the elevation anomalies (h_a) from which we calculate along-track sea surface height anomalies (h_{ssh}), and subsequently estimate freeboard (h_f). Further details of the sea surface height and freeboard calculations are given later in section 4.3 and equations (6) and (7).

4.1. Previous Studies

[21] Derivation of freeboard using ICESat data, via the removal of the marine geoid, has been attempted [e.g., *Forsberg and Skourup*, 2005]. *Kwok et al.* [2006] demonstrated however that such freeboard estimates are contaminated by short-wavelength geoid errors, illustrating that knowledge of the local, instantaneous sea surface height is required for direct retrieval of freeboard. A number of researchers are working toward this aim at present; most work is based on the assumption that the elevation of open water, and/or newly refrozen leads less than a few days old, provides a good representation of the local, instantaneous

sea surface elevation. Elevation measurements of open water and leads can then be used as the reference sea surface height which is subtracted from the elevation of sea ice floes to deduce freeboard. *Kwok et al.* [2007] and *Zwally et al.* [2008] have described a number of techniques to derive freeboard from ICESat data in the Arctic and the Antarctic, respectively.

[22] *Kwok et al.* [2007] provide the following three different approaches for obtaining sea surface height: (1) newly opened leads identified by comparison of ICESat profiles with near-coincident Synthetic Aperture Radar (SAR) imagery, (2) open water or newly refrozen, snow-free, leads indicated by received ICESat pulse reflectivity that is lower than the background average reflectivity, and (3) leads indicated by a local elevation measurement that is lower than that of the surrounding mean surface elevation. While the first method is robust, the disadvantage is that it relies on SAR data in addition to ICESat altimeter data and is time consuming to implement. The advantage of the second and third methods is that they provide a large number of tie points for sea surface height calculation [*Kwok et al.*, 2007], but they each rely on only one ICESat parameter to define lead locations.

[23] *Zwally et al.* [2008] use a method to identify local sea surface that assumes the lowest 2% of ICESat elevations in a 50 km segment represent sea surface elevations. Local sea surface height at any point is calculated by averaging the lowest 2% of elevations within ±25 km of the point. Empirical analysis led to the 2% value being chosen for Antarctic sea ice studies [*Zwally et al.*, 2008]; an equivalent method over Arctic sea ice uses the average of the lowest 1% of elevations within ±50 km of the local data point (D. Yi, personal communication, 2008). The advantage of this method is that it is easily implemented and provides sea surface height measurements for all ICESat elevations. There are however a couple of disadvantages with this method. If no leads or open water are sensed by ICESat in a 50 km segment, then sea surface height is calculated using the average elevation of thinnest sea ice present and is thus overestimated, resulting in freeboards that are incorrectly calculated too low. If, on the other hand, more than 2% of the surface elevation measurements are of open water or refrozen leads, then valid sea surface elevations are discarded. This could result in underestimates of sea surface height, since only the lowest 2% of the valid sea surface elevation data are used. This would result in freeboards incorrectly calculated too high. Since the fixed percentage algorithm does not take into account the seasonally and spatially varying percentage of lead cover across the ice pack it could give rise to biased freeboard estimates.

4.2. Lead Detection Algorithm

[24] We outline a new method to detect leads for the retrieval of altimetric sea surface height in the Arctic Ocean. This method is distinct from those of *Kwok et al.* [2007] and *Zwally et al.* [2008] in that it does not depend on a single parameter to indicate a reflection from a lead, but relies rather on a combination of ICESat parameters including surface elevation, reflectivity, and the properties of the reflected laser waveform, to discriminate leads within the ice pack. Our aim is to first classify those elevation measurements associated with reflections from leads, defined here as open water or newly refrozen leads with snow-free, thin ice surfaces. We will then use these elevations to determine the along-track reference sea surface height required for the calculation of freeboard.

4.2.1. Parameters Defining Waveform Shape

[25] In clear atmospheric conditions, we expect the shape of the received pulse reflected from a lead, which has a smooth surface (e.g., open water, or thin newly refrozen sea ice) and negligible slope, to be (1) Gaussian in shape and (2) highly correlated with the shape of the transmitted pulse. Furthermore, previous analyses by *Kwok et al.* [2006, 2007] suggested that both the elevation and reflectivity associated with leads (either open water or snow-free thin ice) are low relative to the surrounding surfaces.

[26] In addition to the parameters (elevation, reflectivity, and gain), which we extract from the ICESat data products (see section 2.1), we derive a number of other parameters that describe the shape of the transmitted (*Tx*) and received (*Rx*) waveforms. First we determine the peak power of the transmitted and received waveforms (*Tx*_max, *Rx*_max), and measure the waveform full width at half maximum (*Tx*_fwhm, *Rx*_fwhm), which is the width of the waveform at half the peak power. *Tx*_fwhm and *Rx*_fwhm are first measured in terms of bin width and then converted to meters (where each bin is 0.15 m wide [*Brenner et al.*, 2003]). We then calculate the difference between the transmitted and received waveform widths (Δfwhm) as

$$\Delta\text{fwhm} = Rx\_\text{fwhm} - Tx\_\text{fwhm}. \tag{3}$$

[27] We also calculate the skewness of the transmitted and received waveforms (*Tx*_skew, *Rx*_skew). Skewness describes the degree of asymmetry of the waveform about the mean distribution. We define skewness following *Brenner et al.* [2003, p. 33, equation (15)]. We calculate the difference between the transmitted and received waveform skewness (Δskew) as

$$\Delta\text{skew} = Rx\_\text{skew} - Tx\_\text{skew}. \tag{4}$$

[28] Finally, we calculate the cross correlation between the transmitted and received waveforms ($X\text{correl}_{TxRx}$). $X\text{correl}_{TxRx}$ is an indication of the similarity between the received and transmitted waveforms; $X\text{correl}_{TxRx}$ would be 1 for perfectly Gaussian transmitted and received waveforms, or for a waveform crossed with itself. Following *Box and Jenkins* [1976], we derive the cross correlation as follows: given two series $Tx_1, Tx_2, \ldots, Tx_n$ and $Rx_1, Rx_2, \ldots, Rx_n$, of length n, the cross correlations, for a maximum lag L, between Tx_i and the lagged values of Rx_i, are calculated by

$$X\text{correl}_{TxRx}(l) = \sum_{i=1}^{n-l} \left(Tx_i - \overline{Tx}\right)\left(Rx_{i+l} - \overline{Rx}\right)/nS_{Tx}S_{Rx},$$
$$l = 0, 1, \ldots, L, \tag{5}$$

where $\overline{Tx} = \sum_{i=1}^{n} Tx_i/n$, $S_{Tx} = \sqrt{\sum_{i=1}^{n}\left(Tx_i - \overline{Tx}\right)^2/n}$, and similarly for $\overline{Rx}$ and S_{Rx}.

[29] In total, six parameters are used in our analysis of ICESat data. The reflectivity of the waveform indicates a

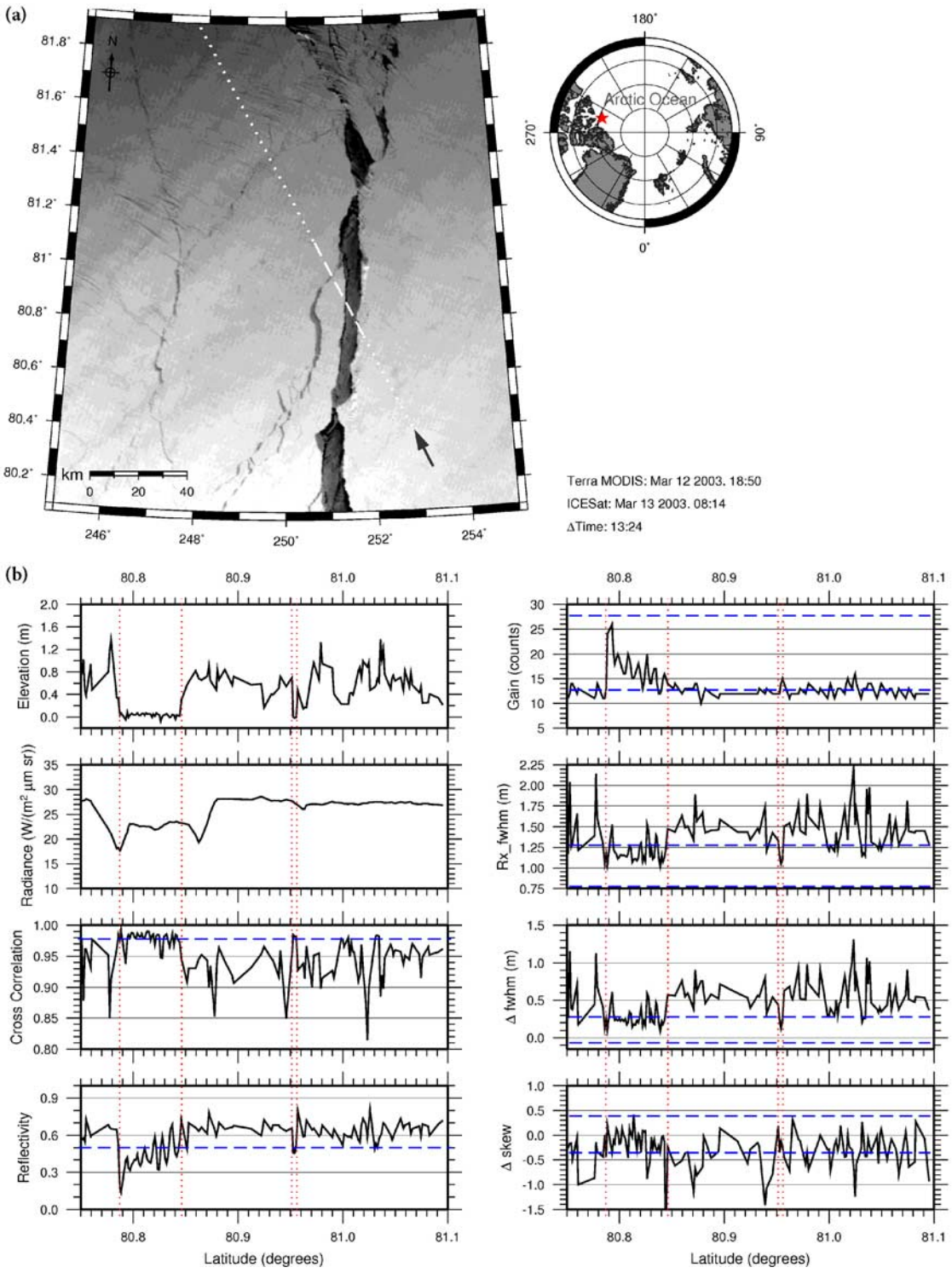

Figure 2. Comparison of ICESat parameter profiles with near-coincident satellite imagery. (a) ICESat track (white dotted line) overlaid on MODIS image showing a well-defined, vertical lead; arrow indicates ICESat flight direction. Inset shows geolocation of comparison north of the Queen Elizabeth Islands (red star). (b) Profiles of ICESat elevation, cross correlation ($X\text{correl}_{TxRx}$), reflectivity, gain, received pulse full width at half maximum (Rx_fwhm), full width at half maximum difference (Δfwhm), skewness difference (Δskew), and the MODIS radiance in the area of the two major leads (white dotted line in Figure 2a) are shown. Position of the two major leads are indicated on the parameter profiles by vertical red dotted lines. The lead identification thresholds described in Table 3 are indicated by horizontal dashed blue lines.

Table 2. Ranges for ICESat Parameters Associated With Leads in Near-Coincident Satellite Imagery[a]

ICESat Overpass	Satellite Image Acquisition	ΔTime (hours)	Xcorrel$_{TxRx}$	Reflectivity	Gain (counts)	Rx_fwhm (m)	Δfwhm (m)	Δskew
13 Mar. 2003, 0505	13 Mar. 2003, 0005	5.0	0.975–0.992	0.25–0.45	11–22	0.98–1.20	0.05–0.30	−0.30–0.30
13 Mar. 2003, 0814	12 Mar. 2003, 2201	10.2	0.975–0.990	0.13–0.48	12–26	1.02–1.20	0.11–0.26	−0.25–0.25
9 Mar. 2003, 1050	9 Mar. 2003, 2155	11.1	0.975–0.990	0.25–0.50	11–21	0.98–1.25	0.00–0.30	−0.60–0.20
7 Mar. 2005, 0436	7 Mar. 2005, 0814	3.6	0.975–1.000	0.15–0.48	13–27	0.80–0.90	−0.06–0.08	−0.30–0.30
1 Mar. 2004, 1410	3 Mar. 2004, 1258	46.8	0.976–1.000	0.16–0.47	13–28	0.90–1.05	−0.06–0.08	−0.30–0.45

[a]Unless units are given, parameters are dimensionless.

low (lead) or high (sea ice or snow cover) albedo surface, the cross correlation (Xcorrel$_{TxRx}$) parameter indicates a reflection from smooth or rough topography within the footprint, the gain value delineates cloud-free returns, and the waveform shape parameters (Rx_fwhm, Δfwhm, and Δskew) indicate the presence or lack of waveform broadening because of surface topography (combined with the spacecraft off-nadir pointing angle) or atmospheric forward scattering. In section 4.2.2, we investigate the behavior of these parameters over sea ice and lead surfaces, with the ultimate aim of determining a set of criteria that can be used to discriminate leads within the along-track ICESat elevation data.

4.2.2. Image Analysis

[30] We analyzed ICESat profiles of elevation, reflectivity, gain and the parameters describing waveform shape (see section 4.2.1), in combination with near-coincident, cloud-free MODIS images of well-defined leads within the ice pack. Satellite imagery is an ideal way of observing the ice pack since the high contrast in albedo between leads and sea ice floes allows for easy identification of each. Figure 2 illustrates an example of the image analysis. Figure 2a shows a MODIS image acquired on 12 March 2003, north of the Queen Elizabeth Islands. The linear black features crossing the image represent regions of low radiance, a characteristic of leads which occur within the higher albedo ice pack (light gray and white areas). Overlaid on the image is the geolocation of a near-simultaneous ICESat pass (white dotted line in Figure 2a). ICESat data gathered along a 6.275 s segment of this pass (denoted by the white dashed line in Figure 2a) are illustrated in Figure 2b. This segment contains 251 ICESat footprints, of which 30 were removed under the filtering scheme (c.f. section 3). The profile of MODIS surface radiance along the ICESat track indicates the location of the two major leads traversed by the satellite, which are low (18–24 W m^{-2} μm^{-1} sr^{-1}) relative to the background radiance of the ice pack (~27–29 W m^{-2} μm^{-1} sr^{-1}). The characteristics of the data associated with the leads (bounded by red dotted lines) indicate that, with respect to the surrounding sea ice floes, leads are associated with low surface elevation, low reflectivity, high gain, and highly correlated transmitted and received waveforms that have low or negligible difference in skewness and waveform full width at half maximum.

[31] We repeated the analysis using a set of five MODIS images (not shown) acquired in different areas of the Arctic Ocean, identifying the location of leads in the along-track profiles of the ICESat data and noting the range of values for each parameter (given in section 4.2.1) at the lead locations. The range of values associated with each parameter is given in Table 2. A total of thirty leads were analyzed as part of this process. The parameter ranges in Table 2 were used to develop a set of criteria for discriminating laser returns from leads and these criteria are presented in Table 3. All criteria must be satisfied for a waveform to be classified as a return from a lead. The parameter thresholds given in Table 3 are included in the Figure 2b as blue dashed lines. We refer the reader to *Farrell* [2007] which documents the satellite images and along-track ICESat data examined as part of this analysis.

4.3. Freeboard Calculation

[32] The along-track sea surface height (the reference surface used in the calculation of sea ice freeboard) is computed by averaging the elevation estimates associated with individual leads that are identified by the lead detection algorithm. For each along-track data point, we calculate the sea surface height (h_{ssh}) by averaging lead elevation estimates (h_L) which are within a 35 km along-track search range of the local data point

$$h_{\mathrm{ssh}} = (1/N)\sum_{i=1}^{N} h_L, \tag{6}$$

where N is the number of return pulses within the along-track search range that fulfill the lead detection criteria (Table 3). Sea surface height measurements depend on at least one ($N \geq 1$) lead detection within the along-track search range, i.e., in the absence of a lead within the along-track search range, no sea surface height measurement is made, and freeboard is not estimated. For a lead which is sampled by more than one ICESat footprint, each return within the lead that is identified by the detection algorithm contributes to the along-track sea surface height estimate. The greater the number of leads detected in each 35 km segment, the better the estimate of local sea surface height. Occasionally the lead detection algorithm will misidentify a surface elevation as a lead (a "false positive") resulting in a lead elevation estimate that is higher than other lead elevations within the segment. We discard such false positives before calculating h_{ssh}. Short-wavelength noise in

Table 3. Criteria for Discriminating Leads in Arctic Pack Ice[a]

Criterion	Threshold
Cross-correlation	$0.975 \leq X\mathrm{correl}_{TxRx} \leq 1$
Reflectivity	$0 \leq$ i_reflctUncorr ≤ 0.5
Gain (counts)	$13 \leq$ i_gainSet1064 ≤ 28
Rx_fwhm (m)	$0.80 \leq Rx\_\mathrm{fwhm} \leq 1.28$
Δfwhm (m)	$-0.08 \leq \Delta\mathrm{fwhm} \leq 0.30$
Δskew	$-0.3 \leq \Delta\mathrm{skew} \leq 0.3$

[a]All criteria must be met for a waveform to be classified as a return from a lead. Unless units are given, parameters are dimensionless.

the along-track sea surface height estimates is reduced by applying an along-track low-pass filter, of filter width 3 km. Finally, ICESat freeboard (h_f) is calculated for each laser shot as the difference between the instantaneous sea ice surface elevation anomalies (h_a) and the averaged along-track sea surface height (h_{ssh})

$$h_f = h_a - h_{ssh}. \quad (7)$$

4.4. Algorithm Validation

[33] Using a second set of five MODIS images, we validated the lead detection algorithm. Again cloud-free MODIS images, with clearly defined leads and open water, were chosen for the validation analysis. Figures 3 and 4 are two examples of the validation (from the set of five) and illustrate the ability of the lead detection algorithm to discriminate leads in the winter (Figure 3a) and autumn (Figure 4a) ice pack in different areas of the Arctic. Red circles along the ICESat ground track (black dashed line) indicate ICESat echoes identified by the algorithm as surface reflections from leads. Lead detection was considered successful if the ICESat echoes identified by the algorithm could be associated with leads in the MODIS image (i.e., locally low radiance values). A total of 25 individual leads can be visually identified in the MODIS imagery (Figures 3a and 4a), of which 16 were successfully identified by the lead detection algorithm. When the complete validation data set is considered, approximately 50% of leads were identified by the lead detection algorithm.

[34] We selected images where the elapsed time to the ICESat overpass of the scene was minimized so as to avoid the impact of ice drift on the validation. The time difference between MODIS image acquisition and ICESat overpasses of the survey regions was 47 min for Figure 3, and 2.75 h for Figure 4. Despite this there is some evidence of misregistration between the MODIS and ICESat data. For example, at 72.3°N–129.6°W in Figure 4, MODIS surface reflectance is high ($\sim$70 W m^{-2} μm^{-1} sr^{-1}) indicating an ice floe, while ICESat elevation and reflectivity are both low relative to the along-track average indicating a lead surface. The inconsistency may either be due to (1) ice drift or divergence of the ice pack during the time that elapsed between the ICESat overpass and image acquisition or (2) since the ICESat footprint is higher resolution than the MODIS image (70 m versus 250 m), ICESat may profile narrow leads that the MODIS sensor would miss.

[35] Inspection of the MODIS images show that the lead locations (red circles) coincide with the presence of leads in the ice pack, especially at the site of largest leads around 82.4°N 50.5°E and 82.55°N 49.7°E in Figure 3a, and around 73.4°N −130.7°W in Figure 4a. A local elevation high, at 82.44°N 50.02°W, within the large lead in Figure 3a, is associated with a small ice floe in the MODIS scene. In general the ICESat elevation data and the MODIS radiance, extracted from the image along the ICESat track, are in excellent agreement with areas of low elevation coinciding with low radiances. Figures 3b and 4b illustrate the local sea surface height and freeboard estimates. The blue line in the top profile of Figures 3b and 4b illustrates the along-track local sea surface computed using the lead elevations (red circles), following equation (6). Freeboard, calculated using equation (7), is shown in the bottom profile of Figures 3b and 4b. The ICESat along-track reflectivity and MODIS radiance profiles are also included to aid the reader's identification of leads within the ice pack.

[36] The validation analysis indicates that not all leads along the ICESat tracks are identified by the lead detection algorithm. For example, although the region between 73.03°N–130.4°W and 73.52°N–130.5°W in Figure 4a has low along-track elevation and low radiance values in the MODIS image, suggesting a lead $\sim$55 km long, not all surface elevations within this segment are classified as leads by the algorithm. In this region 35% of the data have been discarded by the data filtering scheme described in section 3, while other waveforms did not fit the lead criteria (see Table 3), for example 43 % of the surface returns had reflectivity values >0.5. Indeed we found that reflectivity was highly variable, with values between 0.1 and 1.0, within this large lead (as well as within the large lead in Figure 3a). This is not consistent with the assumption that surface returns from leads and thin snow-free ice are associated with low values of reflectivity. We suggest that this is in part due to a lag in the automatic gain control (AGC) loop of the onboard detector in the GLAS instrument. Since the reflectivity measurement is calculated as the received pulse energy scaled by gain [see *Brenner et al.*, 2003] a lag in the AGC over surfaces with rapidly changing albedo can lead to inaccurate estimates of surface reflectivity. In this case, abrupt changes between the albedo of snow covered sea ice floes and open water or thin gray ice, can result in anomalously high values of reflectivity. These examples indicate that, by itself, reflectivity can be a weak indicator of leads along ICESat profiles. Here we have chosen to use reflectivity in conjunction with other parameters to discriminate thin sea ice and leads, but future development of the algorithm may include a lesser dependence on the reflectivity measurements. Furthermore while the lead detection algorithm should ideally discriminate all reflections from leads and thin ice, we note that a small number of lead elevation estimates (h_L) identified with confidence in this study can still be used to obtain a reasonable estimate of the along-track sea surface height. The blue lines, in the top profiles of Figures 3b and 4b, show that equation (6) had produced a smooth h_{ssh} profile for the calculation of freeboard.

5. Arctic Freeboard

[37] The lead detection algorithm, described in section 4.2, was used to process data gathered during the 11 ICESat campaigns outlined in Table 1 and freeboards were estimated following the procedure outlined in section 4.3. Figure 5 illustrates the geographical distribution of waveforms classified as leads by the lead detection algorithm for two ICESat campaigns (FM05 and ON05). Lead detections were ubiquitous across the Arctic Ocean, and 0.5% and 0.9% of the entire data set were classified as leads for the FM05 and ON05 campaigns, respectively. As noted earlier, lead fraction is typically higher during the autumn than in the winter, and as expected, more leads were detected during the autumn campaigns. There was an absence of lead detections in the vicinity of extensive land fast ice (e.g., south of the New Siberian Islands) and small ice shelves. This impacted our

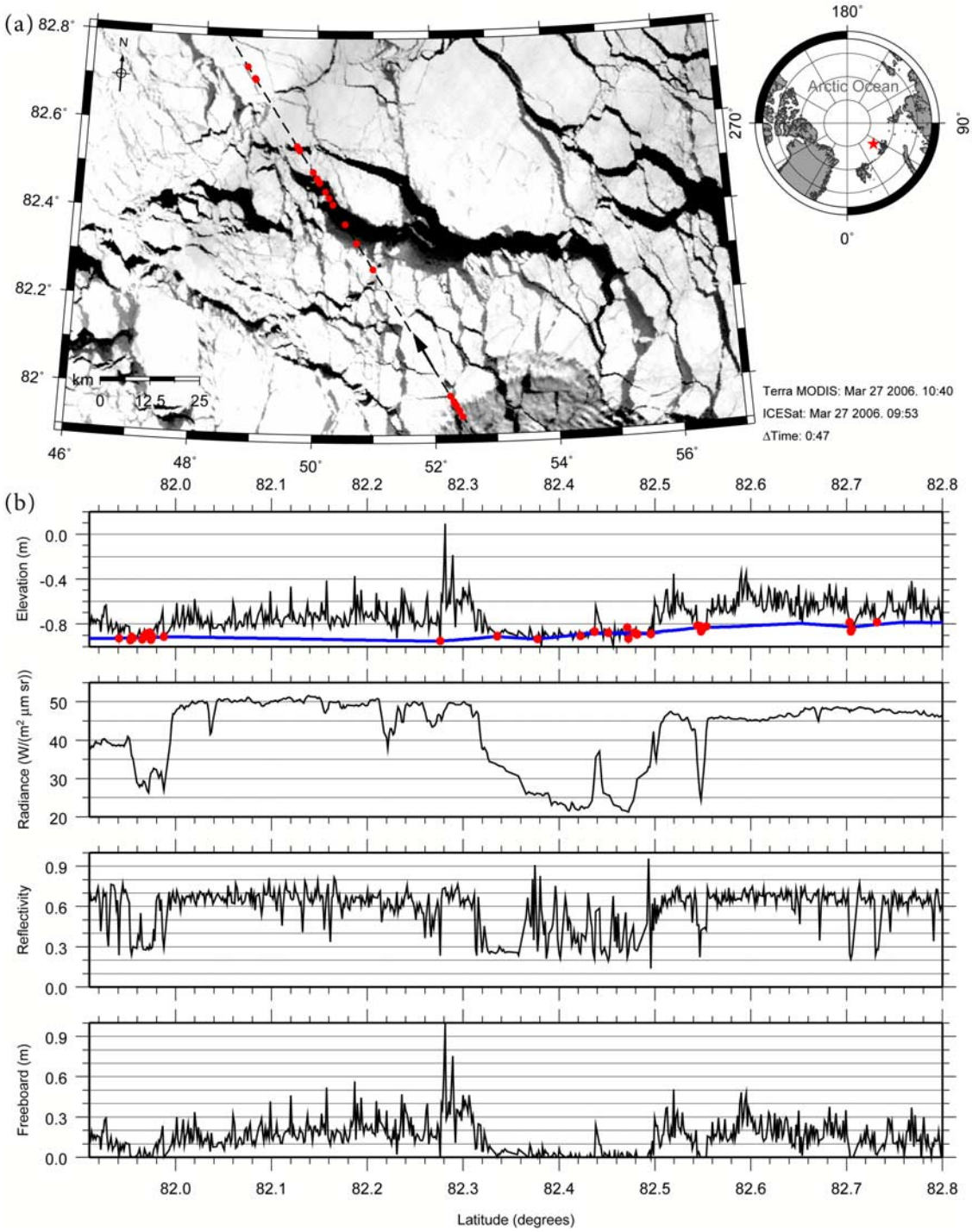

Figure 3. (a) Comparison of lead locations (red circles) identified along an ICESat track (black dashed line) acquired on 27 March 2006 overlaid on near-coincident MODIS imagery; arrow indicates ICESat flight direction. Inset shows geolocation of comparison (red star) north of Franz Josef Land. (b) Profiles of ice surface elevation, local sea surface height (blue line), MODIS radiance, reflectivity, and estimated freeboard along the ICESat track.

ability to calculate freeboard in these regions, since we cannot estimate freeboard in areas where we do not have an estimate of local sea level. Furthermore, since sea ice and ocean waveforms were used in this analysis (GLA01 short waveforms), as opposed to land and ice sheet waveforms (GLA01 long waveforms), we do not obtain freeboard measurements within land-masked areas (e.g., some parts of the Canadian Arctic Archipelago and off the northern coast of Greenland).

[38] Freeboard estimates for the autumn and winter ICESat campaigns between March 2003 and 2008 were averaged into 50 × 50 km grid cells and mapped using a polar

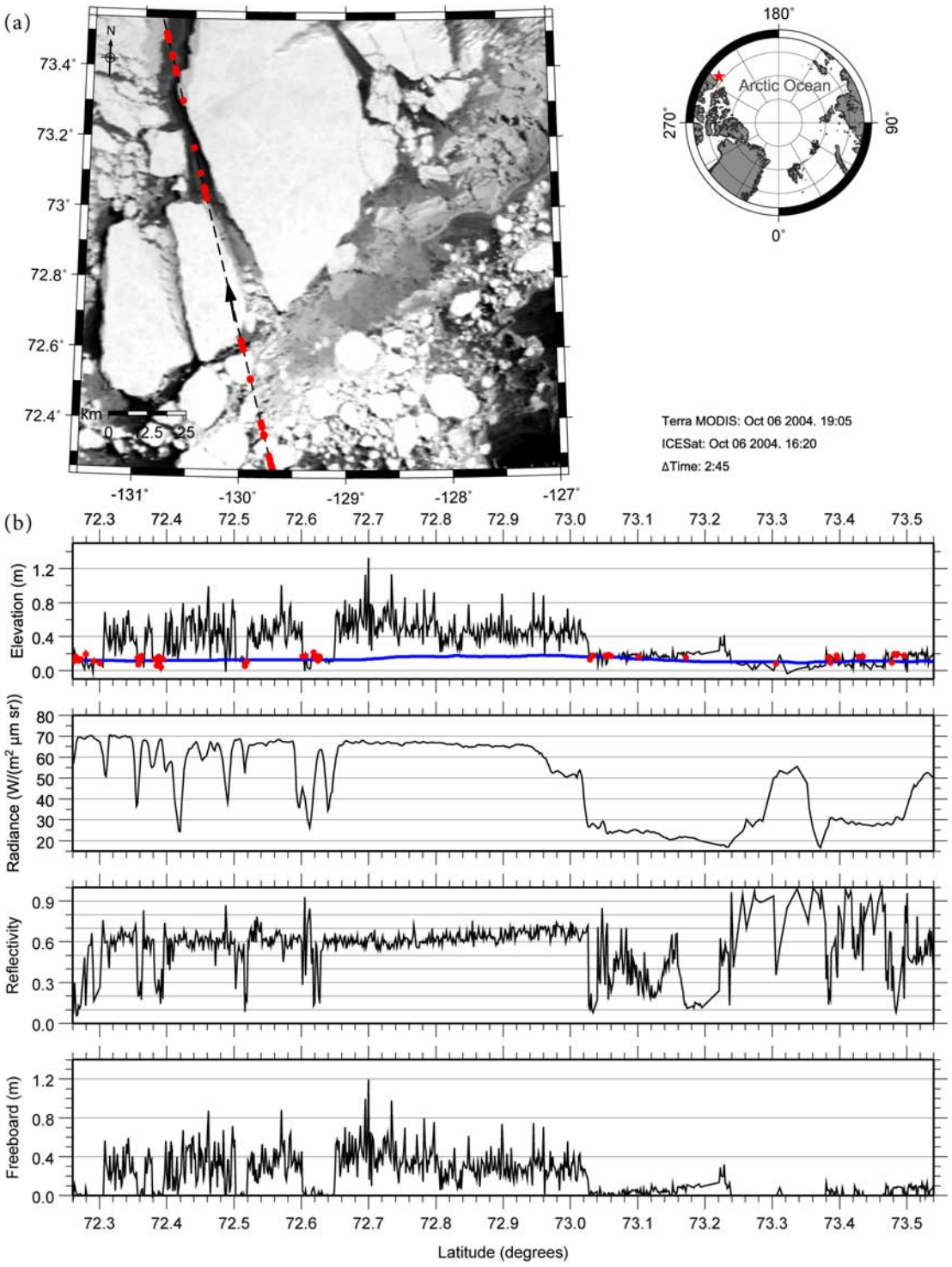

Figure 4. (a) Comparison of lead locations (red circles) identified along an ICESat track (black dashed line) acquired on 6 October 2004 overlaid on near-coincident MODIS imagery; arrow indicates ICESat flight direction. Inset shows geolocation of comparison (red star) near Banks Island. (b) Profiles of ice surface elevation, local sea surface height (blue line), MODIS radiance, reflectivity, and estimated freeboard along the ICESat track.

stereographic projection (Figures 6 and 7). The total number of freeboard estimates (Npoints) and the number of filled 50 km grid cells (Ncells) for each campaign are given to the top left of each map. The maps provide a complete view of the spatial pattern of freeboard across the sea ice covered regions of the Arctic Basin above 65°N, and up to the limit of ICESat coverage at 86°N. The regional distribution of ice freeboard is in line with the estimated sea ice thickness climatology on the basis of submarine sonar profiles [*Bourke and Garrett*, 1987], as expected. One exception to this is

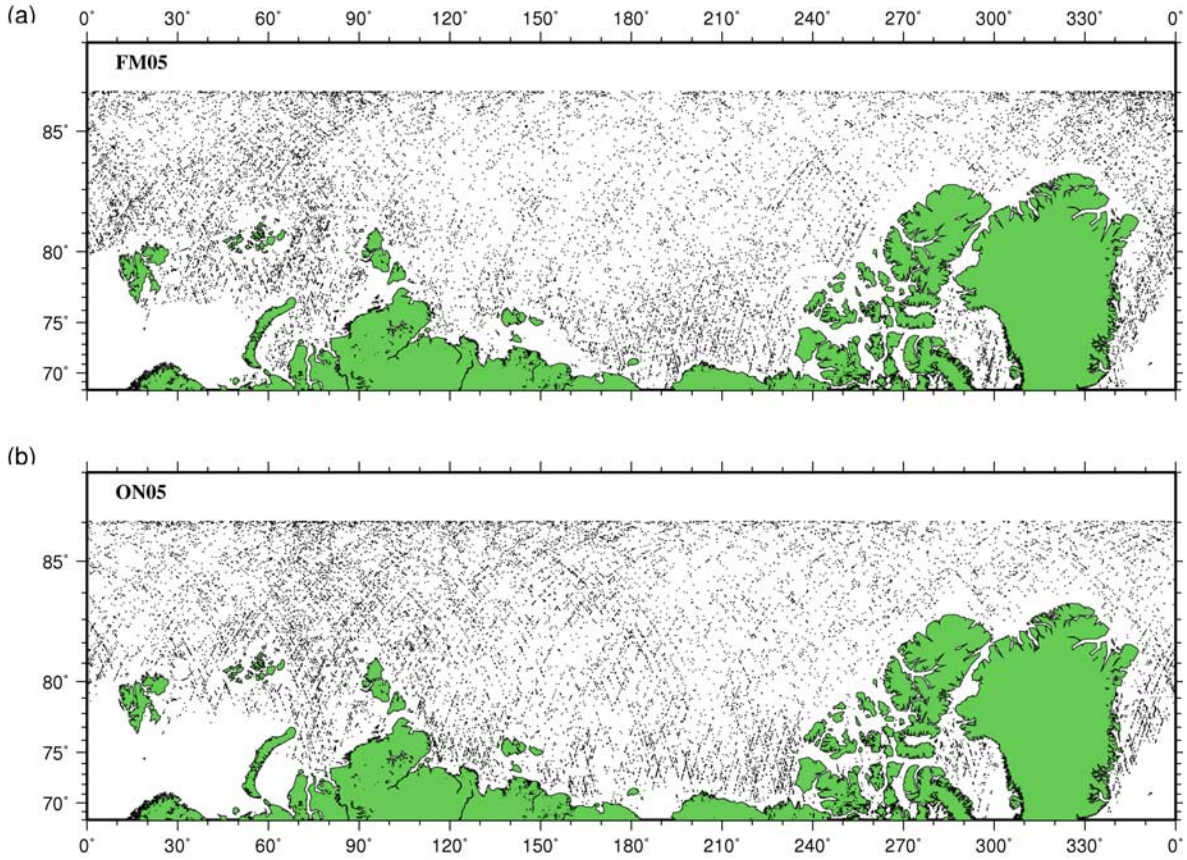

Figure 5. Distribution of leads indentified by the lead detection algorithm (black circles) for the (a) FM05 and (b) ON05 ICESat campaigns, illustrating that lead detections are ubiquitous across the Arctic Basin.

unusually high freeboard estimates (∼35 cm) at the sea ice edge south of Svalbard in the FM08 data set (see Figure 7). Setting a threshold on the minimum number of data points used to estimate sea surface height (and hence freeboard) along the ice edge (e.g., $N \geq 5$, see equation 6) may improve estimates of freeboard in these regions. The thin first-year ice (0–15 cm), recorded during the autumn campaigns (Figure 6), which occur shortly after sea ice minimum, grows into thicker first-year ice (15–30 cm) in the subsequent winter campaign data (Figure 7), which were collected around sea ice maximum. The increase in freeboard represents a combination of ice growth and snow accumulation over the 4-month period between campaigns. Mean freeboard grew by 4.2 cm, 10.2 cm, 9.9 cm, 9.1 cm and 6.7 cm, during the ON03-FM04, ON04-FM05, ON05-FM06, ON06-MA07, and ON07-FM08 campaigns, respectively.

[39] The perennial ice zone (region of multiyear ice, typically found in the high Arctic and north of the Canadian Arctic Archipelago and Greenland coast) can be easily identified in all campaigns (Figures 6 and 7). The perennial ice has a thicker freeboard (∼35–65 cm) and is surrounded by thinner, first-year ice (∼0–30 cm). Using the approximation that the boundary between first-year and perennial ice is ∼35 cm, we have added black contour lines in Figures 6 and 7 to indicate this boundary. The loss of the perennial ice cover of the Arctic has been well documented; a recent study by *Comiso et al.* [2008] states that the trend in perennial ice extent is −10.2% per decade between 1979 and 2007. *Maslanik et al.* [2007] also showed the decline of the oldest Arctic sea ice between 1982 and 2007. In line with these observations, over the 5-year period of ICESat freeboard data shown here, the dramatic loss of the thickest ice cover can clearly be seen. While thicker, perennial ice occupied most of the central Arctic Ocean in the FM03 and ON03 campaigns, the ON07 and FM08 campaign data indicate that perennial sea ice is now confined to a smaller area north of Greenland and Ellesmere Island, and that first year makes up the majority of the ice cover. To illustrate this we consider the ON04 and ON07 campaigns, which are directly comparable since the start and end dates of these campaigns (Table 1) are closest in time. Visual inspection demonstrates that the ON07 perennial ice is thinner and occupies a much smaller area than the ON04 perennial ice freeboard distribution. Furthermore, the late freeze-up period following the September 2007 sea ice minimum, gave rise to a smaller overall areal coverage of the total ice pack during the ON07 campaign compared to the ON04 campaign, including an absence of sea ice in the Chukchi Sea.

[40] The distribution of sea ice freeboard for each ICESat campaign is shown in Figure 8. We computed mean freeboard and standard deviation statistics for each campaign and these are reported in the upper right corner of Figure 8. Our estimates of mean freeboard are in good agreement with those reported by *Kwok et al.* [2007]; for example they give

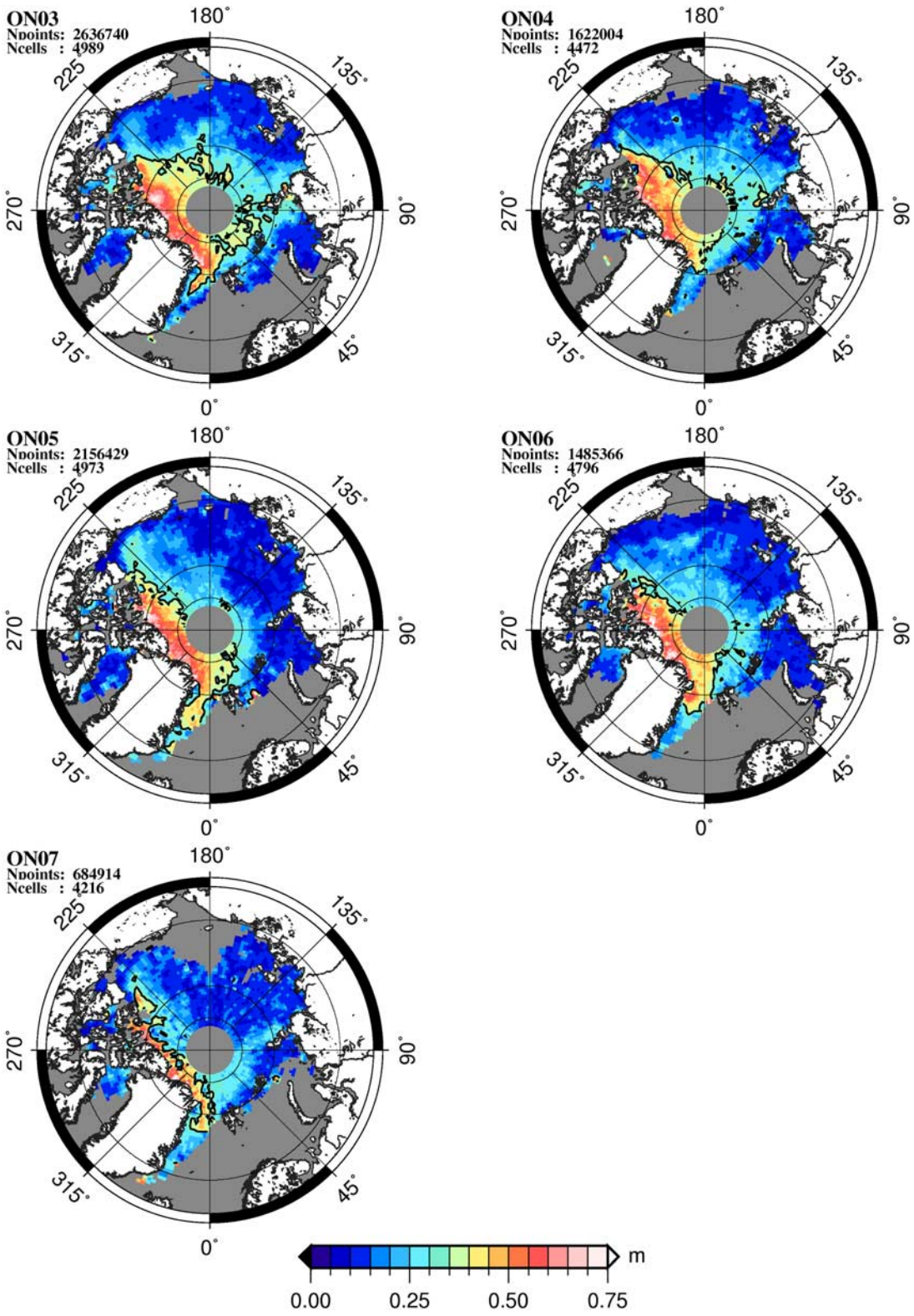

Figure 6. Polar stereographic maps of Arctic freeboard for five autumn ICESat campaigns between 2003 and 2007. The total number of freeboard estimates (Npoints) and the number of filled 50 × 50 km grid cells (Ncells) for each campaign are given to the top left of each map.

freeboard estimates of 27.5 cm and 35 cm for the ON05 and FM06 campaigns, respectively, compared to our estimates of 25 cm and 35 cm. The standard deviation, 14.4 cm on average, represents the variability of the freeboard thickness across the Arctic Basin. The change in the shape of the freeboard distributions over the 5-year period echoes the changes observed in Figures 6 and 7. The distributions are typically bimodal for the earlier campaigns (FM03–FM05)

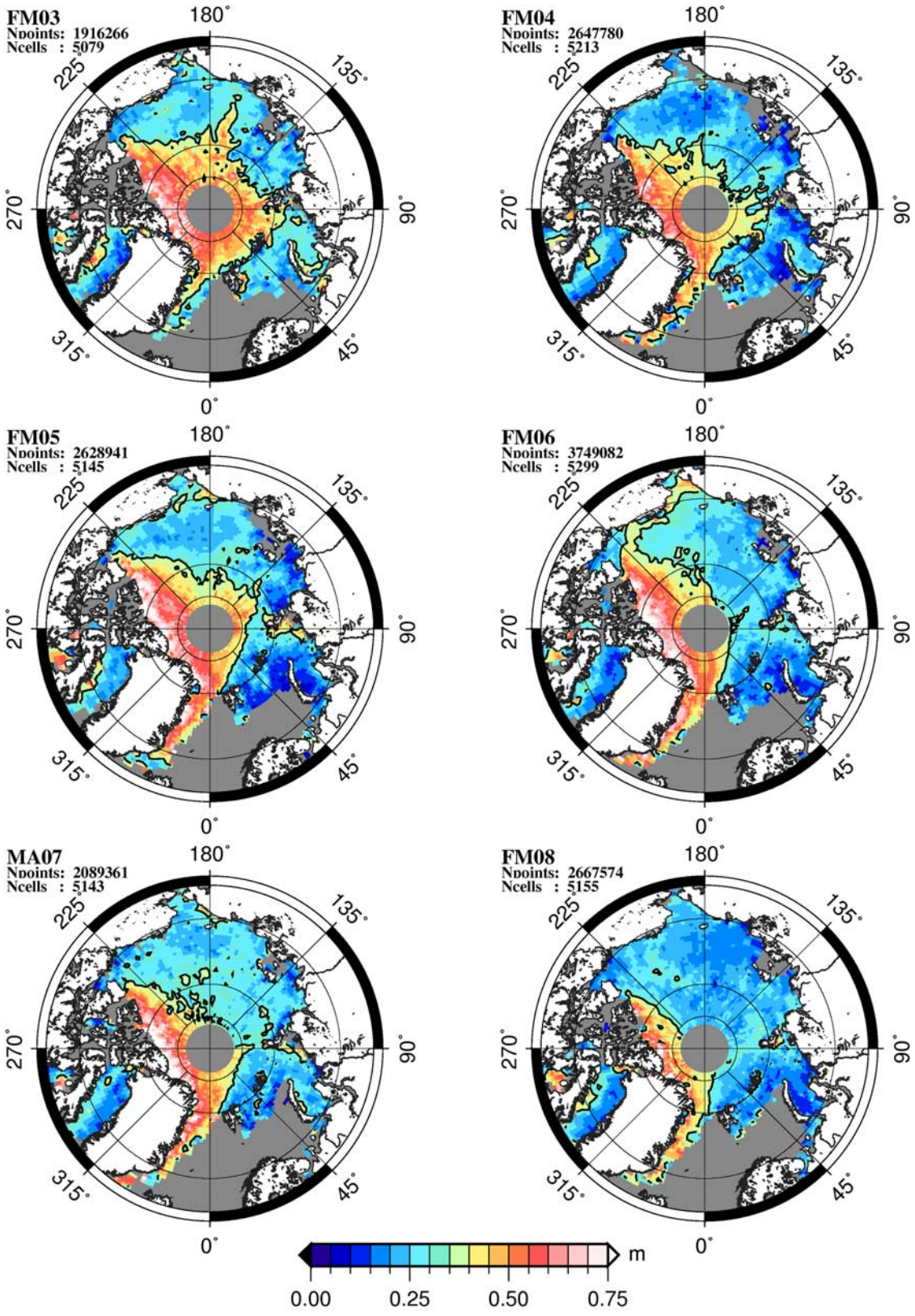

Figure 7. Polar stereographic maps of Arctic freeboard for six winter ICESat campaigns between 2003 and 2008. The total number of freeboard estimates (Npoints) and the number of filled 50 × 50 km grid cells (Ncells) for each campaign are given to the top left of each map.

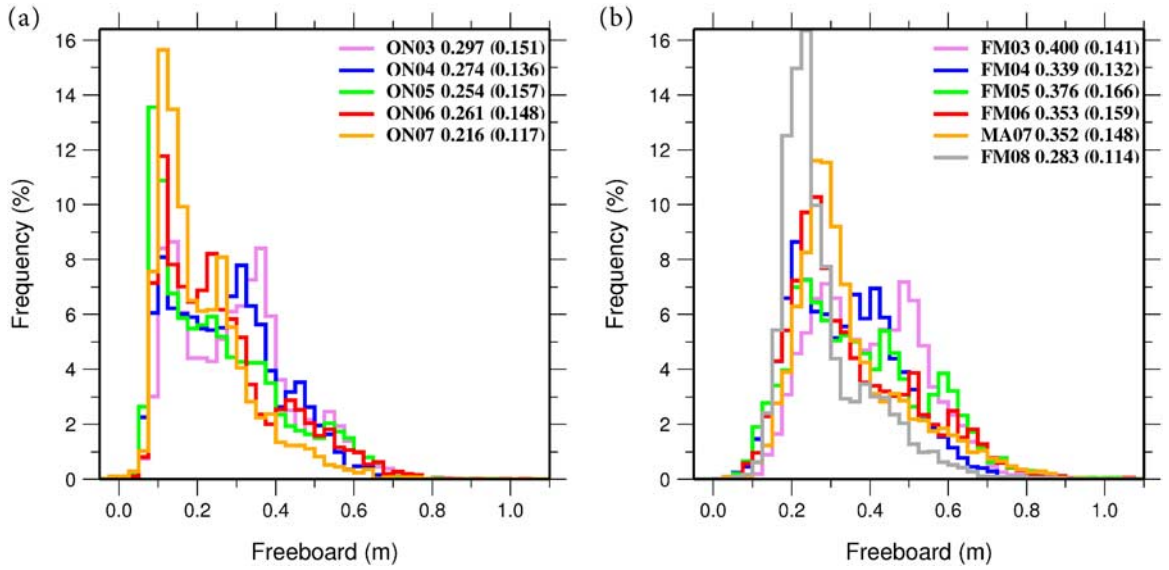

Figure 8. Distributions of freeboard for (a) autumn campaigns and (b) winter campaigns. Mean freeboard and standard deviation (inside brackets) statistics are given, in meters, for each campaign.

with peaks delineating first-year and multiyear ice; for example the FM03 distribution has peaks at 29 cm and 49 cm and the ON03 distribution has peaks at 14 cm and 36 cm. The shift to a thinner ice cover, favoring first-year ice over perennial ice, appears to occur after the previous record sea ice minimum in September 2005 [*Stroeve et al.*, 2008], and the ON05, ON06, and ON07 distributions (Figure 8a) are all sharply peaked around 10 cm. The winter campaign distributions (Figure 8b) typically have long tails, indicating thicker ridged and multiyear ice. The FM08 distribution is however in marked contrast to this, with a sharp peak occurring at 23 cm, a shallower tail indicating further loss of the thicker multiyear ice, and a mean freeboard of 28 cm which is lower than any other winter campaign.

[41] Figure 9 shows a time series of mean freeboard for winter campaigns (blue triangles) and autumn campaigns (green triangles) over the 5-year observation period. Linear regression lines have been fitted to the mean freeboard series and indicate that autumn mean freeboard has declined at a rate of 1.8 cm a^{-1} ($R^2 = 0.86$) and winter mean freeboard at a rate of 1.6 cm a^{-1} ($R^2 = 0.59$). We computed the standard deviation of the data about the trend lines, denoted by σ_y. The autumn mean freeboard data have $\sigma_y = 0.01$ m; despite the small number of data points, the high correlation between

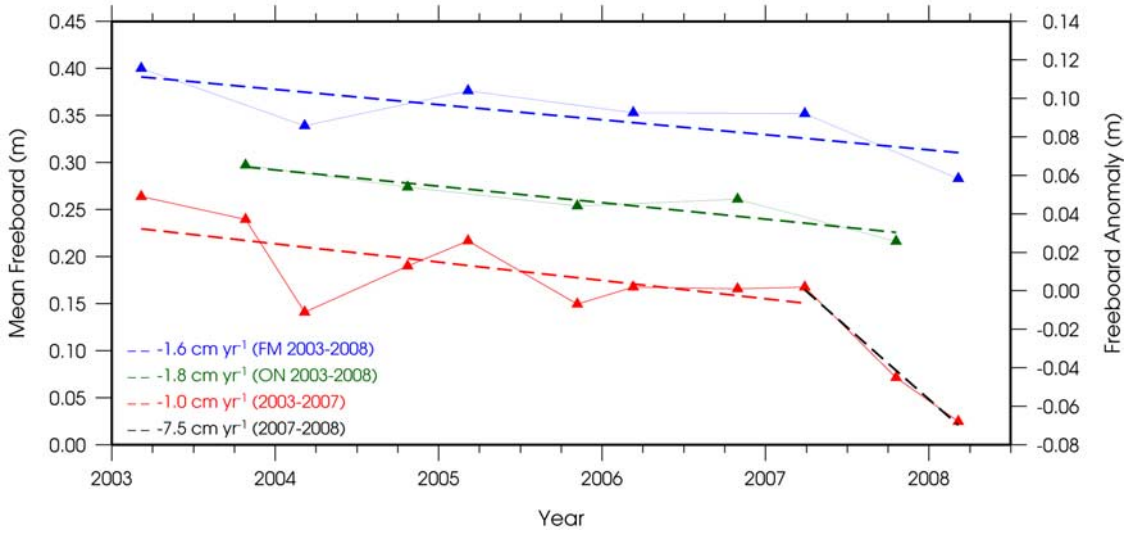

Figure 9. Time series of mean Arctic freeboard for winter campaigns (blue triangles) and autumn campaigns (green triangles), and freeboard anomalies (red triangles) for the period March 2003–2008. Dashed lines are linear regressions that have been fitted to the mean freeboard series and the rates of change are given in the legend at bottom left. Note that the left-hand vertical axis refers to mean freeboard while the right-hand vertical axis refers to the freeboard anomalies about the 2003–2008 mean.

the observations and the trend line, and the small value of σ_y, indicate that the linear model provides a good description of the trend in the data. The winter mean freeboard data have $\sigma_y = 0.03$ m illustrating the interannual variability in mean freeboard, which is superimposed on a decreasing trend. If the rate of change of mean freeboard were constant and continued at the observed rates, extrapolation of these observations indicates that mean freeboard would reach zero by ~2020 on the basis of the autumn data and by ~2027 on the basis of the winter data. However, Figures 6 and 7 suggest that the observed trends primarily reflect the loss of older, thicker, multiyear ice from the Arctic which is being replaced by seasonal first-year ice. A constant continuation of the trend shown here is therefore unlikely and does not take into account future changes in snow loading for a retreating ice cover. In addition annual winter replenishment of the first-year ice pack would preclude a zero winter time mean freeboard in the future.

[42] We found the seasonal, 5-year mean freeboard for the autumn and winter campaigns to be 26 cm and 35 cm respectively. We then calculated a time series of freeboard anomalies where the seasonal mean is subtracted from the mean freeboard for each campaign to produce freeboard anomalies. The freeboard anomalies are indicated by red triangles in Figure 9. Following the September 2007 record minimum sea ice extent, the autumn 2007 and winter 2008 mean freeboards are below the seasonal averages at −4.5 cm, and −6.8 cm, respectively. In addition, the mean winter freeboard dropped by 12 cm between March 2003 and 2008. On the basis of linear regression lines fit to the anomaly time series we have considered the trend in freeboard anomalies over three time periods: the entire observation period (2003–2008), observations before the record sea ice minimum in 2007 (2003–2007), and observations since just before the record sea ice minimum until March 2008 (2007–2008). The following rates of decline were observed: −1.7 cm/a (2003–2008), −1.0 cm/a (2003–2007), and −7.5 cm/a (2007–2008), illustrating the sharp decline in freeboard since 2007.

[43] Interpretation of the decreasing trend in freeboard thickness is not easy since snow depth is part of the freeboard measurement and the variability in ice freeboard and snow thickness superimposed on the ice cannot be separated. However, the interannual variability in snow thickness is estimated to be 2–3 cm [*Laxon et al.*, 2003, and references therein], which is smaller than the observed changes in ICESat freeboard over the observation period. This suggests that the decreasing trend we observe is due to thinning of the sea ice pack, rather than to changes in the snow cover.

6. Summary and Conclusions

[44] NASA's ICESat mission has been in operation now for over 5 years and provides data gathered over ~35–day periods, two or three times per year. We have described a new method for extracting sea surface elevations from ICESat data gathered over the Arctic ice pack and have used this reference surface to calculate sea ice freeboard. The lead detection algorithm relies on analysis of the shape of individual GLAS waveforms and their correlation with the transmitted pulse, as well as on surface reflectivity measurements. We have provided a validation of the lead detection algorithm using near-coincident MODIS imagery, which revealed favorable comparisons between MODIS radiance and ICESat estimates of reflectivity and surface elevation. We have used the laser altimetry data set to estimate Arctic sea ice freeboard from 11 autumn (October–November) and winter (February–March) campaigns spanning March 2003–2008.

[45] We have investigated the seasonal and interannual variability in freeboard during the observation period. We found that mean freeboard increased by ~8 cm on average, during the 4-month period between the autumn and winter campaigns, representing a combination of ice growth and snow accumulation. The 5-year time series indicates a dramatic loss of the thickest sea ice cover: while thick, perennial ice occupied most of the central Arctic Ocean in the earlier campaigns, by the ON07 and FM08 campaigns, the thickest sea ice was not only confined to a small area north of Greenland and Ellesmere Island, but was also thinner than in previous years. Analysis of the distributions of ice freeboard for each campaign further suggests a shift to a thinner ice cover. Whereas the freeboard distributions were typically bimodal for the earlier campaigns (FM03–FM05), with two peaks delineating first-year and multiyear ice, and long tails, indicating thicker, ridged ice, the later freeboard distributions, particularly for the ON05, ON07, and FM08 campaigns, were unimodal and sharply peaked, indicating thinning. We have found that overall sea ice freeboard has decreased during the observation period, in line with reports by others regarding the loss of perennial sea ice. Mean freeboard has declined at a rate of ~1.8 and ~1.6 cm a^{-1} during the autumn and winter periods respectively, in the region above 65°N up to the northern limit of ICESat coverage at 86°N. The autumn 2007 and winter 2008 mean freeboards were below the seasonal averages at −4.5 cm, and −6.8 cm, respectively. The 5-year observation period is too short to definitively say whether these results represent a long-term decreasing trend in Arctic freeboard or are part of a natural variability. Furthermore snow thickness on sea ice remains an unknown contributor to the observed ICESat freeboard variability; interannual variability in snow depth is however estimated to be 2–3 cm, and is therefore smaller than the freeboard changes observed. This suggests that the declining freeboard we observe is due to thinning of the sea ice pack, rather than to changes in the snow cover.

[46] More data from future ICESat campaigns will continue to allow us to examine the state of the ice pack and assess whether it will recover following the sea ice minimum recorded in September 2007. The launch of ESA satellite, CryoSat-2, in late 2009, and the planned ICESat-2 mission, due for launch around 2015, will enable the continued monitoring of the sea ice pack facilitating routine measurements of sea ice freeboard and thickness. The methodology presented here will be useful for future algorithm development for the extraction of sea surface height and sea ice freeboard estimates. In addition to the cryospheric applications presented here, sea surface elevation data have been used in combination with radar altimetry data to map marine gravity anomalies [*McAdoo et al.*, 2008], and will also be used to study the mean dynamic topography of the Arctic Ocean. Future work should include

an investigation of differences between freeboard estimates reported using the several algorithms now available for processing ICESat elevation data over sea ice. Additional validation of the sea ice freeboards presented here will be conducted using Airborne Topographic Mapper (ATM) laser altimetry data, including data gathered during a dedicated validation campaign in March 2006 over sea ice in the Canada Basin [*Connor et al.*, 2007]. We will also compare coincident ICESat laser altimetry data and Envisat radar altimetry data to investigate whether the decreasing freeboard signal described here is common to both data sets, and whether combining such data will allow us to better understand variability in the snow depth of Arctic sea ice and its effect on thickness estimates from satellite altimetry.

[47] **Acknowledgments.** We gratefully acknowledge NASA's ICESat Science Project and the NSIDC for distribution of the ICESat data (see http://nsidc.org/data/icesat/). We thank Laury Miller of the NOAA Laboratory for Satellite Altimetry and Andy Ridout of the Centre for Polar Observation and Modeling, UCL, for their helpful advice and discussions. We also thank both the Associate Editor and two anonymous referees for their most careful and helpful reviews. Support for SLF has been provided by the National Research Council, Research Associateship 0625390, under funding from the National Oceanographic and Atmospheric Administration (NOAA) and previously under National Environment Research Council studentship NER/S/A/2002/10425. The views, opinions, and findings contained in this report are those of the authors and should not be construed as an official National Oceanic and Atmospheric Administration or U.S. Government position, policy, or decision.

References

Arctic Climate Impact Assessment (2005), *Arctic Climate Impact Assessment*, 1042 pp., Cambridge Univ. Press, Cambridge, U. K.

Bourke, R. H., and R. P. Garrett (1987), Sea ice thickness distribution in the Arctic Ocean, *Cold Reg. Sci. Technol.*, *13*, 259–280, doi:10.1016/0165-232X(87)90007-3.

Box, G. E. P., and G. M. Jenkins (1976), *Time Series Analysis: Forecasting and Control*, 545 pp., Holden-Day, London.

Brenner, A. C., et al. (2003), Derivation of range and range distributions from laser pulse waveform analysis for surface elevations, roughness, slope and vegetation heights, *Geosc. Laser Altimeter Syst. Algorithm Theor. Basis Doc. Version 4.1*, 92 pp., NASA, Greenbelt, Md.

Chelton, D. B., J. C. Ries, B. J. Haines, L. L. Fu, and P. S. Callahan (2001), Satellite altimetry, in *Satellite Altimetry and Earth Sciences: A Handbook of Techniques and Applications*, *Int. Geophys. Ser.*, vol. 69, edited by L.-L. Fu and A. Cazenave, pp. 1–131, Academic, London.

Comiso, J. C., and C. L. Parkinson (2004), Satellite-observed changes in the Arctic, *Phys. Today*, *57*(8), 38–44, doi:10.1063/1.1801866.

Comiso, J. C., C. L. Parkinson, R. Gersten, and L. Stock (2008), Accelerated decline in the Arctic sea ice cover, *Geophys. Res. Lett.*, *35*, L01703, doi:10.1029/2007GL031972.

Connor, L. N., S. L. Farrell, W. B. Krabill, D. C. McAdoo, and C. Martin (2007), Validating ICESat Freeboard Estimates of Arctic Sea Ice With Airborne Topographic Mapper (ATM) Observations, *Eos Trans. AGU*, *88*(52), Fall Meet. Suppl., Abstract C11B-0419.

Farrell, S. L. (2007), Satellite laser altimetry over sea ice, Ph.D. thesis, 224 pp., Univ. College London, London.

Forsberg, R., and H. Skourup (2005), Arctic Ocean gravity, geoid and sea-ice freeboard heights from ICESat and GRACE, *Geophys. Res. Lett.*, *32*, L21502, doi:10.1029/2005GL023711.

Fricker, H. A., A. Borsa, B. Minster, C. Carabajal, K. Quinn, and B. Bills (2005), Assessment of ICESat performance at the salar de Uyuni, Bolivia, *Geophys. Res. Lett.*, *32*, L21S06, doi:10.1029/2005GL023423.

Giles, K. A., S. W. Laxon, D. J. Wingham, D. W. Wallis, W. B. Krabill, C. J. Leuschen, D. McAdoo, S. S. Manizade, and R. K. Raney (2007), Combined airborne laser and radar altimeter measurements over the Fram Strait in May 2002, *Remote Sens. Environ.*, *111*, 182–194, doi:10.1016/j.rse.2007.02.037.

Gill, A. E. (1982), Atmosphere-Ocean Dynamics, *Int. Geophys. Ser.*, vol. 30, 662 pp., Academic, London.

Holland, M. M., and C. M. Bitz (2003), Polar amplification of climate change in coupled models, *Clim. Dyn.*, *21*, 221–232, doi:10.1007/s00382-003-0332-6.

Holloway, G., and T. Sou (2002), Has Arctic sea ice rapidly thinned?, *J. Clim.*, *15*, 1691–1701, doi:10.1175/1520-0442(2002)015<1691:HASIRT>2.0.CO;2.

Johannessen, O. M., et al. (2004), Arctic climate change: Observed and modelled temperature and sea-ice variability, *Tellus Ser. A*, *56*, 328–341, doi:10.1111/j.1600-0870.2004.00060.x.

Kenyon, S., and R. Forsberg (2001), Arctic Gravity Project: A status, *Gravity, Geoid and Geodynamics 2000*, vol. 123, edited by M. G. Sideris, pp. 391–395, Springer, New York.

Krabill, W., E. Frederick, S. Manizade, C. Martin, J. Sonntag, R. Swift, R. Thomas, W. Wright, and J. Yungel (1999), Rapid thinning of parts of the Southern Greenland ice sheet, *Science*, *283*, 1522–1524, doi:10.1126/science.283.5407.1522.

Kwok, R., and G. F. Cunningham (2002), Seasonal ice area and volume production of the Arctic Ocean: November 1996 through April 1997, *J. Geophys. Res.*, *107*(C10), 8038, doi:10.1029/2000JC000469.

Kwok, R., and G. F. Cunningham (2008), ICESat over Arctic sea ice: Estimation of snow depth and ice thickness, *J. Geophys. Res.*, *113*, C08010, doi:10.1029/2008JC004753.

Kwok, R., H. J. Zwally, and D. Yi (2004), ICESat observations of Arctic sea ice: A first look, *Geophys. Res. Lett.*, *31*, L16401, doi:10.1029/2004GL020309.

Kwok, R., G. F. Cunningham, H. J. Zwally, and D. Yi (2006), ICESat over Arctic sea ice: Interpretation of altimetric and reflectivity profiles, *J. Geophys. Res.*, *111*, C06006, doi:10.1029/2005JC003175.

Kwok, R., G. F. Cunningham, H. J. Zwally, and D. Yi (2007), Ice, Cloud, and land Elevation Satellite (ICESat) over Arctic sea ice: Retrieval of freeboard, *J. Geophys. Res.*, *112*, C12013, doi:10.1029/2006JC003978.

Laxon, S. W., N. Peacock, and D. Smith (2003), High interannual variability of sea ice thickness in the Arctic region, *Nature*, *425*, 947–949, doi:10.1038/nature02050.

Lemke, P., et al. (2007), Observations: Changes in snow, ice and frozen ground, in *Climate Change 2007: The Physical Science Basis. Contribution of Working Group I to the Fourth Assessment Report of the Intergovernmental Panel on Climate Change*, edited by S. Solomon et al., pp. 337–383, Cambridge Univ. Press, Cambridge, U.K.

Leuschen, C. J., R. N. Swift, J. C. Comiso, R. K. Raney, R. D. Chapman, W. B. Krabill, and J. G. Sonntag (2008), Combination of laser and radar altimeter height measurements to estimate snow depth during the 2004 Antarctic AMSR-E Sea Ice field campaign, *J. Geophys. Res.*, *113*, C04S90, doi:10.1029/2007JC004285.

Lindsay, R., and D. Rothrock (1995), Arctic sea ice leads from advanced very high resolution radiometer images, *J. Geophys. Res.*, *100*(C3), 4533–4544, doi:10.1029/94JC02393.

Luthcke, S. B., D. D. Rowlands, T. A. Williams, and M. Sirota (2005), Reduction of ICESat systematic geolocation errors and the impact on ice sheet elevation change detection, *Geophys. Res. Lett.*, *32*, L21S05, doi:10.1029/2005GL023689.

Maslanik, J., and J. Stroeve (2007), DMSP SSM/I daily polar gridded brightness temperatures, http://nsidc.org/data/nsidc-0001.html, Natl. Snow and Ice Data Cent., Boulder, Colo.

Maslanik, J. A., C. Fowler, J. Stroeve, S. Drobot, H. J. Zwally, D. Yi, and W. J. Emery (2007), A younger, thinner Arctic ice cover: Increased potential for rapid, extensive sea ice loss, *Geophys. Res. Lett.*, *34*, L24501, doi:10.1029/2007GL032043.

Maykut, G. (1978), Energy exchange over young sea ice in the central Arctic, *J. Geophys. Res.*, *83*(C7), 3646–3658, doi:10.1029/JC083iC07p03646.

McAdoo, D. C., S. L. Farrell, S. W. Laxon, H. J. Zwally, D. Yi, and A. L. Ridout (2008), Arctic Ocean gravity field derived from ICESat and ERS-2 altimetry: Tectonic implications, *J. Geophys. Res.*, *113*, B05408, doi:10.1029/2007JB005217.

Osterkamp, T. E., and V. E. Romanovsky (1999), Evidence for warming and thawing of discontinuous permafrost in Alaska, *Permafrost Periglacial Proc.*, *10*, 17–37, doi:10.1002/(SICI)1099-1530(199901/03)10:1<17::AID-PPP303>3.0.CO;2-4.

Rigor, I. G., R. L. Colony, and S. Martin (2000), Variations in surface air temperature observations in the arctic, 1979–97, *J. Clim.*, *13*, 896–914.

Rothrock, D. A., Y. Yu, and G. A. Maykut (1999), Thinning of the Arctic sea ice cover, *Geophys. Res. Lett.*, *26*(23), 3469–3472, doi:10.1029/1999GL010863.

Schutz, B. E., H. J. Zwally, C. A. Shuman, D. Hancock, and J. P. DiMarzio (2005), Overview of the ICESat mission, *Geophys. Res. Lett.*, *32*, L21S01, doi:10.1029/2005GL024009.

Smith, D. M. (1998), Recent increase in the length of the melt season of perennial Arctic sea ice, *Geophys. Res. Lett.*, *25*, 655–658, doi:10.1029/98GL00251.

Stroeve, J., M. M. Holland, W. Meier, T. Scambos, and M. Serreze (2007), Arctic sea ice decline: Faster than forecast, *Geophys. Res. Lett.*, *34*, L09501, doi:10.1029/2007GL029703.

Stroeve, J., M. Serreze, S. Drobot, S. Gearheard, M. Holland, J. Maslanik, W. Meier, and T. Scambos (2008), Arctic sea ice extent plummets in 2007, *Eos Trans. AGU*, *89*(2), 13–14, doi:10.1029/2008EO020001.

Wadhams, P., and R. J. Horne (1980), An analysis of ice profiles obtained by submarine sonar in the Beaufort Sea, *J. Glaciol.*, *25*, 401–424.

Yi, D., H. J. Zwally, and X. Sun (2005), ICESat measurement of Greenland Ice Sheet surface slope and roughness, *Ann. Glaciol.*, *42*, 83–89, doi:10.3189/172756405781812691.

Zwally, H. J., et al. (2002), ICESat's laser measurements of polar ice, atmosphere, ocean and land, *J. Geodyn.*, *34*, 405–445, doi:10.1016/S0264-3707(02)00042-X.

Zwally, H. J., D. Yi, R. Kwok, and Y. Zhao (2008), ICESat measurements of sea ice freeboard and estimates of sea ice thickness in the Weddell Sea, *J. Geophys. Res.*, *113*, C02S15, doi:10.1029/2007JC004284.

S. L. Farrell and D. C. McAdoo, NOAA Laboratory for Satellite Altimetry, 1335 East-West Highway, Silver Spring, MD 20910-3282, USA. (sinead.farrell@noaa.gov)

S. W. Laxon, Centre for Polar Observation and Modelling, University College London, Gower Street, London WC1E 6BT, UK.

D. Yi and H. J. Zwally, Cryospheric Sciences Branch, Goddard Space Flight Center, Code 614.1, Greenbelt, MD 20771, USA.